

# The MUSIC of Galaxy Clusters III: Properties, evolution and Y-M scaling relation of protoclusters of galaxies

Federico Sembolini<sup>1,2\*</sup>, Marco De Petris<sup>2</sup>, Gustavo Yepes<sup>1</sup>, Emma Foschi<sup>2</sup>, Luca Lamagna<sup>2</sup>  
Stefan Gottlöber<sup>3</sup>

<sup>1</sup>*Departamento de Física Teórica, Módulo C-15, Facultad de Ciencias, Universidad Autónoma de Madrid, 28049 Cantoblanco, Madrid, Spain*

<sup>2</sup>*Dipartimento di Fisica, Sapienza Università di Roma, Piazzale Aldo Moro 5, 00185 Roma, Italy*

<sup>3</sup>*Leibniz-Institut für Astrophysik, An der Sternwarte 16, 14482 Potsdam, Germany*

Accepted XXXX . Received XXXX; in original form XXXX

## ABSTRACT

In this work we study the properties of protoclusters of galaxies by employing the MUSIC set of hydrodynamical simulations, featuring a mass-limited sample of 282 resimulated clusters with available merger trees up to high redshift, and we trace the cluster formation back to  $z = 1.5, 2.3$  and 4. We study the features and redshift evolution of the mass and the spatial distribution for all the cluster progenitors and for the protoclusters, which we define as the most massive progenitors of the clusters identified at  $z = 0$ . A natural extension to redshifts larger than 1 is applied to the estimate of the baryon content also in terms of gas and stars budgets: no remarkable variations with redshift are discovered. Furthermore, motivated by the proven potential of Sunyaev-Zel'dovich surveys to blindly search for faint distant objects, we focus on the scaling relation between total object mass and integrated Compton  $y$ -parameter, and we check for the possibility to extend the mass-observable paradigm to the protocluster regime, far beyond the redshift of 1, to account for the properties of the simulated objects. We find that the slope of this scaling law is steeper than what expected for a self-similarity assumption among these objects, and it increases with redshift mainly for the synthetic clusters where radiative processes, such as radiative cooling, heating processes of the gas due to UV background, star formation and supernovae feedback, are included. We use three different criteria to account for the dynamical state of the protoclusters, and find no significant dependence of the scaling parameters from the level of relaxation. Based on this, we exclude that the dynamical state is the cause of the observed deviations from self-similarity.

**Key words:** methods: numerical – galaxies: clusters – cosmology – cosmology: theory – cosmology : miscellaneous

## 1 INTRODUCTION

The formation of today's large scale structures, from massive clusters to smaller groups of galaxies, starts from high redshift overdensities lying along the dark matter filamentary structure known as the cosmic web. In the early phases of their evolution these objects are characterized by relatively smooth peaks in the spatial distribution of dark matter and galaxies, and grow into denser and larger concentrations of dark matter, gas, and galaxies at later epochs. Therefore, by systematically searching for protoclusters, and studying their dynamics, evolution and abundance as a function of mass and redshift, it is possible to explore the high- $z$  stages of the assembly

of present day clusters, and possibly to shed light on the processes which affect the growth of structures on the tail of the halo mass function just as they shape from small overdensities, on the verge of virialization, into the largest, most massive bound objects in the Universe. The evolution of the halo MF puts constrain on  $\Omega_m$  mass and redshift up to the very early stages of their assembly.

Currently, many observational and theoretical issues impose critical limitations to this kind of studies: distance limits the quantity and accuracy of available observations of these objects. Several direct and indirect approaches have been tried to perform systematic searches of protoclusters in the high- $z$  universe, but none of them has been proved to be generally successful and therefore none has been employed for systematic protocluster searches up to now. (see sec. 2 for a review of current observing methods). A reliable observational proxy for their total mass, which assumes an insight of the structure assembly at high redshift and a proper validation of available proxies, as with low- $z$  clusters and groups,

\* E-mail: federico.sembolini@uam.es

due to the necessity of exploring the mass distribution of protoclusters. Following the same approach of cluster studies performed up to redshift 1 (Sembolini et al. 2013), in this work we explore the possibility to observe protoclusters through the detection of their thermal Sunyaev-Zeldovich (th-SZ, Sunyaev & Zeldovich 1970) imprint into the Cosmic Microwave Background (CMB). Due to the lack of dimming of the scattered CMB photons off ionized gas in the high- $z$  halos, and to the uniqueness of its spectral signature at mm/submm wavelengths, th-SZ effect appears as a viable tool for high- $z$  object-finding, as proved from the success of blind cluster surveys from the current generation of millimeter telescopes (Staniszewski et al. 2009, Marriage et al. 2011, Planck Collaboration et al. 2011, Williamson et al. 2011, Planck Collaboration et al. 2013a, Reichardt et al. 2013). In principle, the high angular resolution and the sensitivity needed to provide reliable SZ detections of farther, fainter, less evolved objects should be at hand, thanks to the upcoming generation of instruments like Mustang2, ALMA, CCAT, SPT3G (among others) or satellite missions like Millimetron<sup>1</sup> or the proposed PRISM<sup>2</sup> (PRISM Collaboration et al. 2013).

Within a self-similar scenario of structure formation, a tight correlation between an aperture-integrated th-SZ signal (which is a measure of the total thermal energy of the hot gas in a large virialized structure) and the total mass  $M$  of the object, is expected. For clusters and groups, this scaling law, and its small deviations from self-similarity, have been studied through semi-analytical approaches (e.g. Shaw, Holder & Bode 2008, Sun et al. 2011) simulations of cosmological volumes (Battaglia et al. 2011, Kay et al. 2012, Sembolini et al. 2013) and verified through observations (Bonamente et al. 2008, Marrone et al. 2012, Planck Collaboration et al. 2013c, Planck Collaboration et al. 2013b, Sifón et al. 2013). In this paper we verify for the first time the extension of the self-similarity assumption to the progenitors of today's clusters. For this purpose we use synthetic objects extracted from a large dataset of hydrodynamical simulations of clusters of galaxies: MUSIC. While the definition of a protocluster is in debate from an observational point of view (details are provided in sec. 3), the availability of numerically simulated structures at all the ages up to  $z = 4$  may allow to trace the evolution of clusters back to the formation through the information of the merging tree for each object. The paper is organized as follows. In Section 2 observational approaches of distant galaxies, assumed as possible progenitors of groups and clusters, are reported. The protoclusters extracted from simulation are described in Section 3, where also the baryons budget is explored in terms of gas and star fractions for different masses and protocluster redshifts. Considerations about the spatial distribution of the progenitors and useful criteria to quantify the virial state of these objects are also treated. The validity of the self-similarity approach, basics for the  $Y - M$  scaling law, is verified in Section 4 for objects ranging from  $z = 1$  up to  $z = 4$ . In Section 5 we summarize and discuss our main results.

## 2 MULTIWAVELENGTH OBSERVATIONS OF PROTOCLUSTERS OF GALAXIES

In order to investigate when and how clusters are formed, it is necessary to obtain a sample of objects at  $z > 1$ . In the past decade,

there has been a significant increase in the study of clusters at redshifts up to 1, while the difficulty of observing protoclusters of galaxies limits the amount and accuracy of the observations and surveys that are available.

In fact, notwithstanding the development of a new generation of telescopes, many observational and theoretical issues impose critical limitations to these kinds of studies. The hindrances in observing protoclusters of galaxies are linked to the relative low angular resolution of the observation instruments used and consequently to the inability to investigate extended structures. Moreover, according to the  $\Lambda$ CDM model, it is extremely rare to find objects with  $M > 3 \times 10^{14} M_{\odot}$  at  $z > 1$  (Springel et al. 2005) and high redshift galaxies do not dominate the number counts in surveys. In addition, X-ray emission becomes too faint to be measured since the surface brightness decreases as  $(1+z)^4$ . Despite these limitations, observations made in the optical/IR wavelengths together with the XMM-Newton have identified an overdensity of galaxies emitting at  $z = 1.579$  in the X-rays band (Santos et al. 2011). Another finding in the survey XDCP (XMM-Newton Distant Cluster Project) led to the identification of a low-mass (proto)cluster ( $M = 10^{14} M_{\odot}$ ) at  $z = 1.1$ , thanks to the multi-band observation with the GROUND imager (Pierini et al. 2012). X-rays observations thus make possible to observe groups and clusters at much earlier stages (i.e.,  $z \geq 1$ ). However, these surveys still remain subject to the selection effects.

The ability to perform systematic searches of protoclusters in the high- $z$  universe has long been sought after. Various methods have been applied in order to render this possible. High redshift galaxies can be distinguished from the profuse nearby galaxies due to some peculiar spectral characteristics. Thanks to these features, it is possible to use other methods of detection in order to investigate the universe at high redshift. One of the methods most widely used is targeting high- $z$  radio galaxies (HzRGs). These are massive star-forming galaxies with enormous radio luminosities (Miley & De Breuck 2008, Seymour et al. 2007, Rocca-Volmerange et al. 2004). According to the model of hierarchical galaxy formation, it is possible to find galaxy overdensities around HzRGs (Stevens et al. 2003, Mayo et al. 2012), which should be likely surrounded by cluster progenitors (Venemans et al. 2007, Kuiper et al. 2010, Hatch et al. 2011, Wylezalek et al. 2013).

Recent results were obtained as part of the HeRGE project. A study of the IR spectral energy distribution of the Spiderweb Galaxy at  $z = 2.156$  showed that this protogalaxy is in a particular phase implying both of AGNs and starburst (Seymour et al. 2012). Moreover, by combining different studies of the environment of this galaxy, it was possible to identify several protocluster members surrounding the host galaxy, with an estimated mass  $> 2 \times 10^{14} M_{\odot}$  within a region of 3 Mpc.

Another approach is based on the selection of the Lyman Break Galaxies (LBGs), which are star-forming galaxies at  $2.5 < z < 5$  characterized by the Lyman break at  $912 \text{ \AA}$  in the rest-frame (Giavalisco 2002). Searching for Ly $\alpha$  emitters is another way to identify galaxy cluster progenitors (Steidel et al. 1998). Star-forming galaxies exhibit strong emissions of this particular line because Ly $\alpha$  photons are resonantly scattered in neutral hydrogen. Using narrow-band imaging, it is possible to search for overdensities of line emitting objects at a specific redshift. Many studies have been conducted using this particular method and have resulted in the discovery of cluster progenitors beyond  $z = 3$  (Matsuda et al. 2009, Steidel et al. 2000, Yamada et al. 2012, Capak et al. 2011).

It is also possible to observe star-forming galaxies by detecting their sub-millimeter emission. In fact, the large and negative

<sup>1</sup> <http://www.sron.rug.nl/millimetron>

<sup>2</sup> <http://www.prism-mission.org>

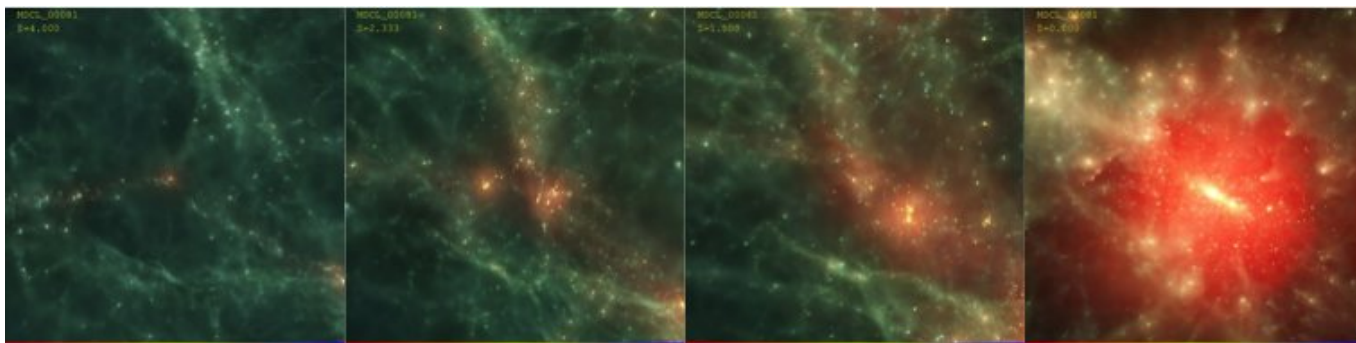


**Figure 2.** The evolution of one of the resimulated regions of MUSIC-2 dataset (CSF run) from high redshift to  $z = 0$  (from left to right:  $z = 4, 2.3, 1.5, 0$ ). At high redshifts the protocluster is located in the top part of the image. All the images of MUSIC clusters have been generated with SPLITCH (Dolag et al. 2008) and are available at the website <http://music.ft.uam.es>.

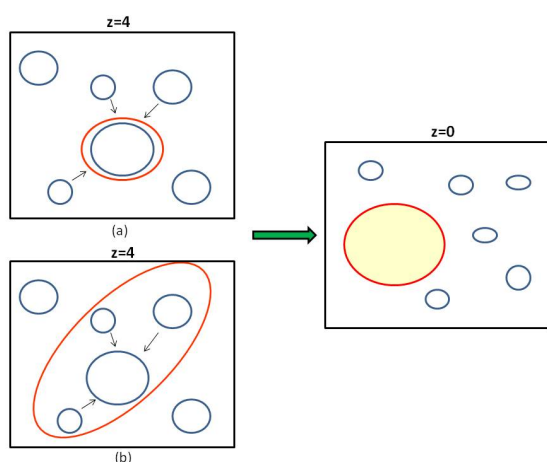


**Figure 1.** Schematic representation of the two protocluster definitions. In the panels on the left, the red circle confines the protocluster at  $z = 4$  according to the first definition (a) and the second (b). In the panel on the right, it is shown the representation of the present-day cluster, which is the main object at  $z = 0$ , formed during the evolution process of the protocluster (according to both definitions).

$k$ -correction (Blain & Longair 1993), due to the steepness of the submm-spectra, makes the high-redshift galaxies more detectable than their low-redshift counterparts. It is possible to identify star-forming galaxy at FIR/submm wavelengths, through the detection of dust emission. Studies of radio galaxies have been concentrated on high redshift objects since their submm luminosity increases with redshift and their emission is in correspondence with the peak of dust emission (Archibald et al. 2001). A population of almost 200 luminous galaxies at  $z > 1$  has been revealed through deep surveys in the submm/mm waveband thanks to detectors such as SCUBA, MAMBO and BOLOCAM (Blain et al. 2002).

Thanks to the current ground-based projects (such as ACT, SPT), it is becoming increasingly possible to observe high- $z$  objects while steadily increasing the redshift through the SZ effect. Recently, it has been made possible to detect clusters at redshift greater than 1 via the Sunyaev-Zel'dovich effect. The SPT-SZ survey allowed the identification of the highest redshift galaxy cluster that was seen via the SZ effect, which is at  $z = 1.478$  (Bayliss et al. 2013).

### 3 PROTOCLUSTERS OF GALAXIES IN THE MUSIC DATASET

Since it is difficult to prove how and when today's clusters of galaxies were formed, what is meant by the term "protocluster" from an observational point of view is in debate. As a result, it is particularly important to be able to discriminate in this study all the high- $z$  objects related to present clusters. With this purpose we define as progenitors all those objects which will merge during the cluster evolution to form and be part, with at least a consistent fraction of their mass (see Sec.3.2), of the cluster observed at  $z = 0$ .

For the purpose of our work, two alternative and general definitions have been used. We assume as a protocluster (Fig.1):

- (i) the most massive halo at high redshift among all the progenitors;
- (ii) the ensemble of all the progenitors with a mass larger than a selected value (which depends on limits on the observability or on the resolution of the simulation)

According to this, numerical simulations constitute the ideal tool to define and study protoclusters: in fact, using a merger tree, it is straight forward to trace back at high redshift the particles, and therefore the progenitors, which will end up into a virialized cluster at  $z = 0$ . This fundamental characteristic allows to overcome the principal problem found in observations, where it is impossible at present day to be completely confident if a massive object observed at high redshift will actually evolve into a cluster during its history.

To the scope of this work, which is to study some integrated properties of protoclusters, we choose to adopt the first definition of the two aforementioned. Most of the analysis shown in this work is referred to protoclusters, though it is also interesting to make some considerations about all the progenitors in terms of their mass and spatial distributions.

#### 3.1 The simulations

The simulations used in this work are part of the MUSIC dataset<sup>3</sup>. A detailed description of the MUSIC dataset can be found in Sembolini et al. (2013), so in this subsection we will limit to recall some main characteristics of the simulations and to define the subset that we selected for our analysis. The protoclusters presented

<sup>3</sup> Initial conditions and snapshots of MUSIC clusters, plus many images, are publicly available at the webpage <http://music.ft.uam.es>

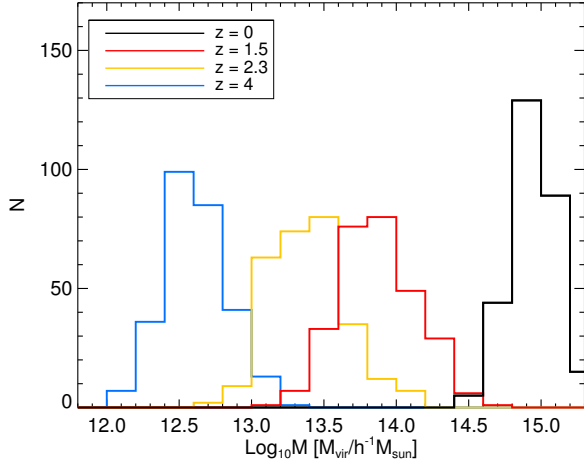


**Figure 3.** Distribution of virial mass of protoclusters at the different analyzed redshifts ( $z = 1.5$  in red,  $z = 2.3$  in yellow,  $z = 4$  in blue), compared with the mass distribution of the same objects evolved into clusters at  $z = 0$  (black).

in this work have been taken from the MUSIC-2 dataset, a mass selected volume limited sample of resimulated clusters extracted from the MultiDark Simulation (MD, Prada et al. 2012). From the MD simulation, a dark-matter only simulation of  $2048^3$  particles in a  $(1h^{-1}\text{Gpc})^3$  cube, all the objects with a total virial mass  $M_{vir} > 10^{15}h^{-1}M_{\odot}$  at  $z = 0$  in the low resolution version of the simulation were selected and resimulated adding SPH and star particles, plus various radiative processes (including radiative cooling, heating processes of the gas arisen from a UV background, star formation and supernovae feedback).

In total, 282 lagrangian regions with a radius of  $6h^{-1}\text{Mpc}$  surrounding a massive cluster were resimulated. All clusters were resimulated, with the same zooming techniques and resolution, both with radiative (CSF subset, see Fig.2) and non-radiative physics (NR subset). The mass resolution for these simulations corresponds to  $m_{DM} = 9.01 \times 10^8 h^{-1}M_{\odot}$  and to  $m_{gas} = 1.9 \times 10^8 h^{-1}M_{\odot}$ . The parallel TreePM+SPH GADGET code (Springel 2005) was used to run all the resimulations. Among the 15 snapshots describing the evolution of each cluster in the redshift range  $0 \leq z \leq 9$ , we concentrate on those corresponding to  $z = 1.5, 2.3, 4.0$ , assuming that at  $z \leq 1$  all objects have already evolved into clusters. The analysis shown hereafter is therefore focused on the protoclusters corresponding to the most massive progenitors of the most massive clusters of each of the 282 MUSIC-2 resimulated regions. Among all the massive clusters at  $z = 0$ , almost 50 per cent have  $M_{vir} > 10^{15}h^{-1}M_{\odot}$  and almost all  $M_{vir} > 5 \times 10^{14}h^{-1}M_{\odot}$ .

### 3.2 Mass and spatial distributions of progenitors and protoclusters

As aforementioned, we can use a merger tree to track back in time the cluster history and individuate all the progenitors (including the protocluster) at high redshifts. We use the merger tree of the Amiga Halo Finder (AHF, Knollmann & Knebe 2009) to select all the high redshift objects containing particles which will be part of a massive cluster at  $z = 0$ , and, according to the definition given at the beginning of this section, we individuate as progenitors all those halos whose at least the 80 per cent of their particles are found to be part of the cluster formed at  $z = 0$ . Considering that AHF is able

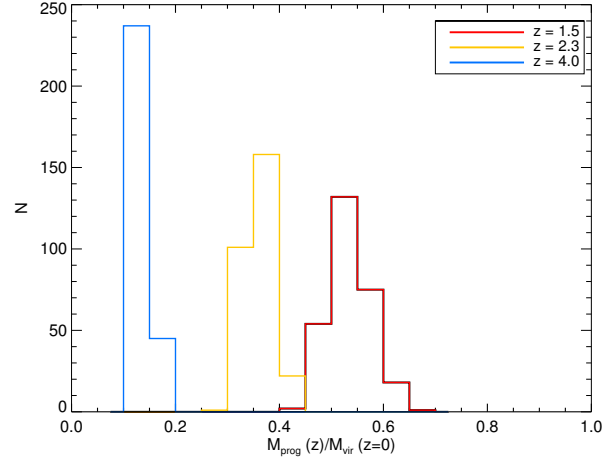


**Figure 4.** Distribution of the mass fraction of the total cluster mass at  $z = 0$  hosted by progenitors with  $M > 1.2 \times 10^{10}h^{-1}M_{\odot}$  at  $z = 1.5$  (red), 2.3 (yellow) and 4 (blue).

to discern all halos constituted by at least 20 particles, we can list all progenitors with  $M > 1.2 \times 10^{10}h^{-1}M_{\odot}$ .

It is interesting to study the mass distribution of protoclusters (calculated at the virial radius) to explore the mass evolution with redshift and to compare the mass of protoclusters with that of the other progenitors, in order to check at each redshift whether the protoclusters show already a mass sensitively bigger than the other progenitors. For each halo the virial radius  $R_{vir}$  is computed, defined as the radius at which the mean internal density is  $\Delta_{vir}$  times the background density of the Universe at that redshift (the value of  $\Delta_{vir}$  therefore depends on redshift too). According to this, the definition of virial mass is<sup>4</sup>:

$$M_{vir} = \frac{4\pi}{3} \Delta_{vir} \Omega_m \rho_{crit} R_{vir}^3 \quad (1)$$

In Fig.3 the distribution of  $M_{vir}$ , at the 3 considered redshifts, is compared with the mass distribution of the evolved clusters at  $z = 0$ . The mass distributions of protoclusters are almost completely separated among each other at the 3 different redshift considered (though showing a large dispersion, see Tab.1): at  $z = 4$  most of halos have a mass of a few times  $10^{12}h^{-1}M_{\odot}$ , with only a small number of objects with  $M > 10^{13}h^{-1}M_{\odot}$ ; at  $z = 2.3$  almost all objects show masses in the range  $10^{13} < M[h^{-1}M_{\odot}] < 10^{14}$ ; at  $z = 1.5$  we find more than 100 halos with  $M > 10^{14}h^{-1}M_{\odot}$  and that therefore can be also considered as already evolved into clusters (if we define as cluster a virialized halo with  $M > 10^{14}h^{-1}M_{\odot}$ ).

The mean value of each mass distribution is reported in Tab.1. It is interesting to measure the fraction of the total mass of the cluster at  $z = 0$  which is contained in the progenitors at high redshift,  $M_{prog}/M(z = 0)$ : we find that at  $z = 4$  only a very small fraction of the total mass (14 per cent, see Tab.1) is hosted by the progenitors, showing how at this age of the Universe most of the matter which will collapse into clusters is still in the form of diffuse matter (i.e. filaments) or of structures under galaxy size; still at  $z = 1.5$  only almost half of the total mass of clusters at  $z = 0$  is still not detected in progenitors with  $M > 1.2 \times 10^{10}h^{-1}M_{\odot}$ . It is also worth

<sup>4</sup>  $\rho_c$  is the critical density of the Universe, defined as  $\rho_c = 3H^2/8\pi G$  ( $H$  is the Hubble constant and  $G$  the gravitational constant)

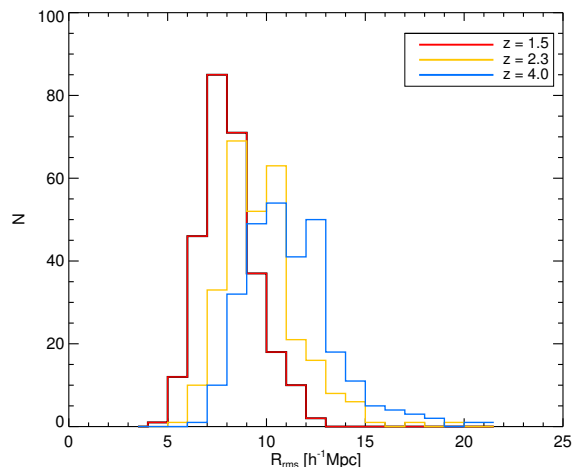


**Figure 5.** Spatial distribution of progenitors in terms of  $rms$  distances at  $z=1.5$  (red), 2.3 (yellow) and 4 (blue), all calculated assuming the center of mass of the protocluster as the center of the cluster formation region.

mentioning that mass ratio between the second most massive progenitor and the protocluster itself is in mean about 70 per cent at  $z = 4$  and still almost 60 per cent at  $z = 1.5$ , an evidence that during their formation history most of massive clusters go through a major merger at  $z > 1$ .

We also concentrate on studying the spatial distribution of progenitors at different redshifts; if we assume the center of the region of the forming cluster as the center-of-mass of the protocluster, we can define the root mean square distance as:

$$R_{rms} = \sqrt{\frac{\sum_{i=0}^N r_i^2}{N}} \quad (2)$$

where  $N$  is the total number of progenitors and  $r_i$  the distance between the  $i$ -th progenitor and the center-of-mass of the protocluster. The distribution of the  $R_{rms}$  at the 3 redshift analyzed is shown in fig.5 and the mean values reported in Tab.1: the initial cluster forming region shows in mean  $R_{rms} \sim 11h^{-1}\text{Mpc}$  at  $z = 4$ , contracted at  $R_{rms} \sim 8h^{-1}\text{Mpc}$  at  $z = 1.5$ . We remind that the typical virial radius at  $z = 0$  of the clusters formed by these regions collapsing is about  $2h^{-1}\text{Mpc}$  and the mean virial radii of our dataset at different redshifts are listed in Tab.1. It is interesting to observe that even if we pull down from 80 to 50 or 20 per cent the threshold of particles of an object which have to be part of the cluster at  $z = 0$  in order to define it as a progenitor, the mean values of the  $R_{rms}$  do not change of more than 5 per cent; we find that the maximum radius (whose mean values are also reported in Tab.1) of the cluster forming area is always  $R_{max} \sim 2R_{rms}$ .

### 3.3 Baryon properties of protoclusters

It is interesting to explore the baryon content of protoclusters of galaxies, in order to follow the evolution of the baryon, gas and star fraction (respectively  $f_b, f_g, f_s$ ) of galaxy clusters in the range  $0 \leq z \leq 4$ ; at the same time, we can check whether our dataset is affected by cold flows or galaxy feedbacks, effects that usually affect the inner regions of clusters but that in the case of such small objects could affect also areas closer to the virial radius. This is important to verify if we want to study integrated properties of protoclusters, such as the integrate Compton parameter  $Y$ , directly de-

	$z = 1.5$	$z = 2.3$	$z = 4.0$
$M_{vir} [10^{13}h^{-1}M_{\odot}]$	$9.2 \pm 6.4$	$3.0 \pm 2.2$	$0.5 \pm 0.3$
$R_{vir} [h^{-1}\text{Mpc}]$	$1.04 \pm 0.22$	$0.72 \pm 0.15$	$0.40 \pm 0.07$
$M_{prog}/M(z=0)$	$0.53 \pm 0.04$	$0.36 \pm 0.02$	$0.14 \pm 0.01$
$R_{rms} [h^{-1}\text{Mpc}]$	$8.1 \pm 1.4$	$9.8 \pm 1.9$	$11.2 \pm 2.3$
$R_{max} [h^{-1}\text{Mpc}]$	$16.1 \pm 2.6$	$19.2 \pm 3.1$	$22.0 \pm 3.7$

**Table 1.** Mean values (at different redshifts) of the virial mass ( $M_{vir}$ ) and virial radius ( $R_{vir}$ ) of protoclusters, of the mass fraction hosted by progenitors with  $M > 1.2 \times 10^{10}h^{-1}M_{\odot}$  ( $M_{prog}/M(z=0)$ ), of  $R_{rms}$  and  $R_{max}$ .

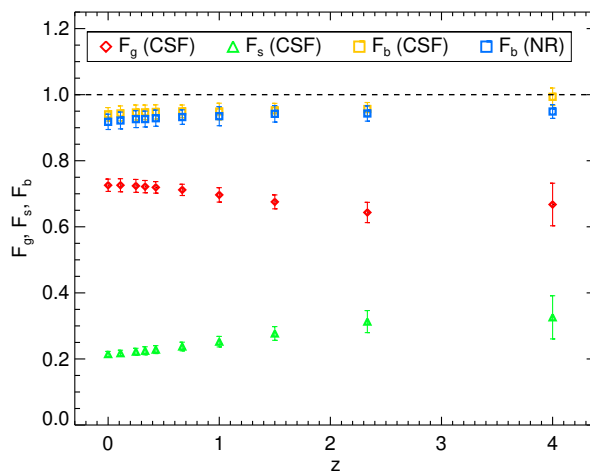


**Figure 6.** Evolution of normalized gas (red diamonds), star (green triangles) and baryon fraction (yellow squares for CSF protoclusters and blue squares for NR) from  $z = 4$  to  $z = 0$ .

pending on the gas content, which has therefore to be described correctly (see Section 4).

The baryon, gas and star fractions are defined by simply taking into account all the gas and star particles falling inside the virial radius:

$$f_{b,g,s}(< R_{vir}) = \frac{M_{b,g,s}(< R_{vir})}{M(< R_{vir})} \quad (3)$$

where  $M_g$  is the mass of the gas,  $M_s$  the mass of the star component, and the total baryon mass is defined as  $M_b = M_g + M_s$ . Fig.6 shows the behavior of the mean baryon, gas and star fractions calculated at the virial radius in the redshift range  $0 \leq z \leq 4$  (results referring to  $z \leq 1$  are taken from Sembolini et al. 2013), normalized to the critical cosmic ratio  $\Omega_b/\Omega_m$ , (which according to the cosmology adopted by MUSIC is 0.174) in order to make a comparison with other works adopting different cosmological parameters (since now on we denote the normalized values of  $f_{b,g,s}$  using capital letters:  $F_{b,g,s}$ ). The normalized  $F_b$  is around 95 per cent at all redshifts for both CSF and NR subsets, as expected slightly higher than what measured in simulations of clusters at  $z \leq 1$  at  $\Delta_c = 500$ ,  $F_{b,500} \sim 0.85$  (Sembolini et al. 2013, Planelles et al. 2013). We remind that  $\Delta_c$  defines that the overdensity is calculated with respect to the mean critical overdensity of the Universe at the redshift analysed. This was easy to predict as the value of the baryon fraction

is expected to approach the cosmic ratio going from inner to outer regions of (proto)clusters and does not vary with redshift.

The gas fraction appears to be lower for protoclusters ( $z \geq 1.5$ ,  $F_g \sim 0.65$ ) than for clusters ( $z \leq 1$ ), for which we find that  $F_g$  is around 75 per cent, values that can be treated as reasonable if we consider that CSF simulations show  $F_g \sim 0.65$  at  $\Delta_c=500$ . The mean value of the normalized star fraction rises from  $F_s \sim 0.2$  at  $z = 0$  to  $F_s \sim 0.3$  at  $z = 4$ , an amount still smaller than what is estimated in the inner regions of clusters (those which are more likely to be affected by cold flows) at  $\Delta_c=2500$ . These results are comforting to the purpose of our analysis, as they allow us to state that there are no dramatic differences in the baryon content between clusters and protoclusters, and we can go on studying the integrated properties depending on gas content of the second ones.

### 3.4 Dynamical state of protoclusters

It is interesting to study the dynamical state of protoclusters in order to check if the morphology of these objects could have an impact on scaling relations. Three different criteria are commonly used to define the morphological state of clusters and protoclusters, aiming at distinguishing relaxed objects from disturbed ones (Shaw et al. 2006, Knebe & Power 2008):

- The presence of mergers, defining as major mergers those objects with a mass bigger than one half of the main object and as minor mergers those objects with a mass between 0.1 and 0.5 times the mass of the main object. Clusters experiencing or having experienced merger processes are more likely to be morphologically disturbed.
- The center-of-mass offset, namely the spatial separation between center-of-mass of the protocluster and the center-of-density (maximum density peak), normalized to the virial radius (see eq.4). Objects showing an high value of  $\Delta r$  are considered disturbed.
- The accomplishment of the virial theorem, calculating the virial ratio  $\eta = 2T/|U|$  (where  $T$  is the kinetic energy and  $U$  the potential energy). If the object is relaxed, we should find  $\eta \sim 1$ .

The first criterium seems not to be successful when applied to protoclusters, as these show merger rate much lower than clusters at low redshift (35 per cent for clusters at  $z < 1$ ).

We have therefore to concentrate on the two other methods to fulfill our purpose of distinguishing relaxed protoclusters from disturbed ones. The center-of-mass offset is quantified as:

$$\Delta r = \frac{|r_\delta - r_{cm}|}{R_{vir}} \quad (4)$$

where  $r_\delta$  is the position of the center-of-density of the halo,  $r_{cm}$  the center-of-mass and  $R_{vir}$  the virial radius.  $\Delta r$  is used to quantify substructures statistics, providing an estimate of the halo's deviations from smoothness and spherical symmetry. Up to now, this topic has been treated in literature in the case of dark-matter only simulations. To identify an halo as a relaxed one the limit value, assigned to  $\Delta r$ , ranges from  $\Delta r \leq 0.04$  (Macciò et al. 2007) to  $\Delta r \leq 0.1$  (D'Onghia & Navarro 2007). Here we will show that hydrodynamical simulations of clusters present higher values of  $\Delta r$  with respect to dark-matter only simulations, so we choose to adopt the highest value among those previously cited:  $\Delta r \leq 0.1$  to define an object as relaxed.

The third and last requirement uses the virial theorem to determine which halos are not dynamically relaxed. The standard definition for a dynamical system in equilibrium is usually represented by  $\eta \sim 1$ . Nevertheless, the effect of those particles situated outside

the virial radius but still gravitationally bound to the halo has to be taken into account and included in the estimate of the kinetic and potential energies. These particles are still bound to the halo and their contribution to the virial theorem has to be considered. The additive term, to include this surface pressure energy at the boundary of the halo, can be quantified as (Chandrasekhar 1961):

$$E_s = \int P_s(r) \mathbf{r} \cdot d\mathbf{S} \quad (5)$$

The measure of the virial ratio  $\eta$  has therefore to be modified to take into account this surface pressure term. Therefore, a modified definition of the virial parameter can be expressed as follows:

$$\eta_1 = \frac{2T - E_s}{|U|} \quad (6)$$

Assuming an ideal gas, the surface pressure can be calculated as (Shaw et al. 2006):

$$P_s = \frac{1}{3V} \sum_i (m_i v_i^2) \quad (7)$$

where  $V$  is the volume of the spherical shell between 0.8 and 1.0  $R_{vir}$  and  $m_i$  and  $v_i$  are the mass and velocity of the  $i$ -th particle respectively. Integrating  $P_s$  over the bounding surface of the halo volume it is found  $E_s = 4\pi r_{med}^3 P_s$ , assuming  $r_{med} \simeq 0.9 R_{vir}$  (Knebe & Power 2008).

We apply this analysis, already performed by Knebe & Power (2008) and Power, Knebe & Knollmann (2012) to dark-matter (DM) only halos, to our hydrodynamically simulated protoclusters, in order to check any dependence between halos mass, virial ratio and center-of-mass offset.

In the case of CSF objects, we find a mild dependence between the mass of the progenitor at different redshifts,  $M_z$ , and virial ratio  $\eta_1$  (see Fig.10):

$$\eta_1 \propto M_z^{0.04} \quad (8)$$

It is interesting to notice how this mass dependence is not fulfilled by NR clusters (Fig.10, bottom panel).

The numerical values of  $E_s$  are generally almost one order of magnitude smaller than the kinetic energy. The correction due to the surface pressure makes therefore the value of the virial ratio lower, but in most cases not enough to reach the expected value of 1.

In Fig.7 we represent the relation between the two definitions of virial ratio,  $\eta$  and  $\eta_1$ , computed both for CSF (top panel) and NR (bottom panel) subsets, for the same redshift bins we previously considered. At  $z = 4$ , the extent of the range covered by the virial ratio for CSF protoclusters is much larger than in the NR case, having clusters with values closer to  $\eta_1 = 1$ , that is expected for relaxed objects. On the contrary, NR clusters at all redshifts present a behavior of the virial ratios with no differences with redshift, none of them having values smaller than 1.2, regardless of whether the pressure term is considered or not. At lower redshifts ( $z = 1.5$ ) higher mean values of  $\eta$  and  $\eta_1$  are found for CSF clusters, confirming the mass dependence of the two parameters, and there are no significant differences between CSF and NR subsets. Therefore, we conclude that the effect of the effective pressure term computed as mentioned above, underestimate the contribution of bound particles outside our definition of virial radius<sup>5</sup>. Nevertheless, it is interesting to see that there are some high- $z$  protoclusters

<sup>5</sup> In the AHF halo finder, the *virial* radius of the halos is defined as the radius that encompasses a mean density that fulfills the numerical solution of the spherical top hat model at that redshift



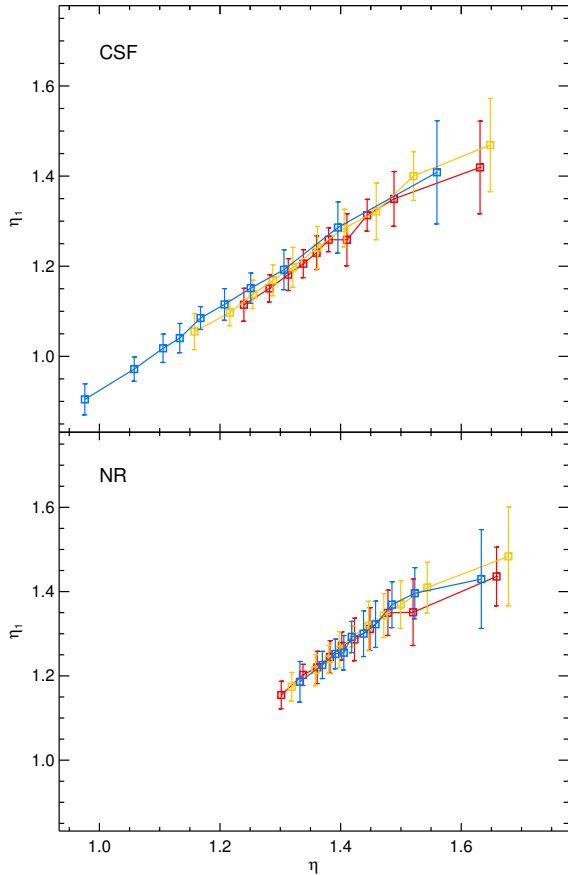


**Figure 7.**  $\eta_1 - \eta$  relation for CSF protoclusters (top panel) and NR protoclusters (bottom panel):  $z=1.5$  is red,  $z=2.3$  is yellow and  $z=4$  is blue. In the CSF relation there is a linear dependence between the two parameters; objects at redshift  $z=1.5$  show lower values of  $\eta, \eta_1$ , reflecting the  $\eta_1 - M$  linear dependence: objects at  $z=1.5$  have bigger masses and therefore higher  $\eta_1$  values. NR protoclusters exhibits the same linear dependence than CSF objects, but the values of  $\eta$  are distributed on a narrower range at high values.

in CSF simulations that do follow the virial theorem, even without correction for pressure terms.

We finally explore the relation between the two criteria adopted here to define the dynamical state of halos, virial ratios ( $\eta, \eta_1$ ) and center-of-mass offset ( $\Delta r$ ). In Fig.8 we show the relation between the average values of  $\eta_1$  (and  $\eta$ ) CSF and NR protoclusters at different redshift bins  $\Delta r$ . There is a clear relation between the two dynamical state estimators. The virial ratios flatten off for values of  $\Delta r \leq 0.1$  and start to increase when  $\Delta r \geq 0.1$ . Therefore this confirms the validity of both criteria to study the dynamical state of simulated halos. According to these results, we simply define those protoclusters of our dataset with  $\Delta r \leq 0.1$  as relaxed halos, classifying as disturbed all halos showing a higher value. Therefore, about 30% of protoclusters appear to be disturbed for the whole redshift interval considered.

As we already pointed out before, it is also clear from Fig.8 that CSF protoclusters present values of  $\eta_1$  much closer to 1 than NR protoclusters, while at lower redshift this difference is much less evident. This is better seen in Fig.9 where we compare the  $\eta_1$  as a function of  $\Delta r$  for CSF and NR for high (upper panel) and low redshifts (lower panel). This behavior is reflecting the different

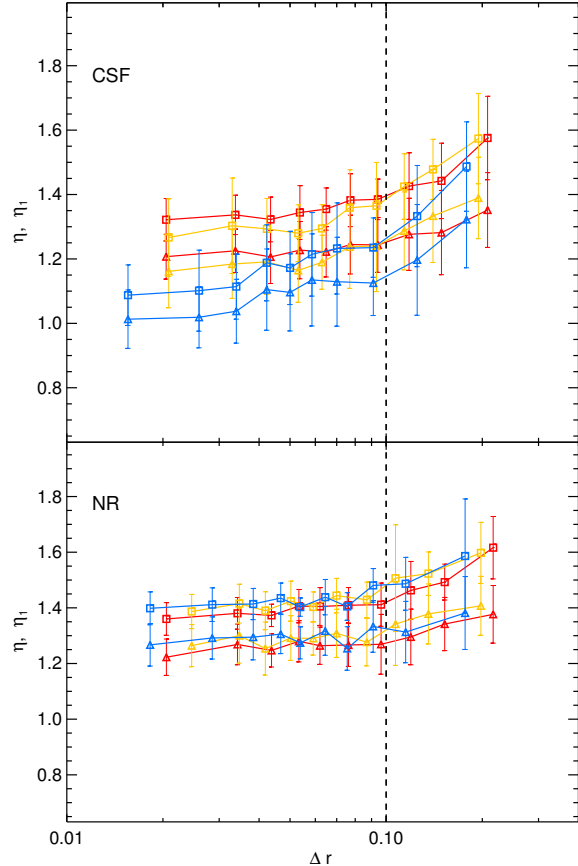


**Figure 8.** Relation between the two definitions of virial ratio  $\eta$  (squares) and  $\eta_1$  (triangles) and the center-of-mass offset  $\Delta r$  at different redshifts ( $z=1.5$  in red,  $z=2.3$  in yellow,  $z=4$  in blue) for the CSF (top panel) and NR (bottom panel) subsets. The vertical black dashed line indicates the upper value to define relaxed halos ( $\Delta r = 0.1$ ).

ways of mass growth of halos at different redshifts. At high redshift the major accretion of matter to halos is by smooth accretion through filaments (Kereš et al. 2005, Madau, Diemand & Kuhlen 2008). In the case of CSF halos, the infalling cooled gas is able to overcome the accretion shocks and makes its way towards the center of protoclusters, forming stars efficiently (Birnboim & Dekel 2003, Dekel et al. 2009), deepening the potential well. Since most of the accretion is smooth, no major source of kinetic energy is injected to the protoclusters, and thus, the matter rapidly virializes in the deeper potentials of CSF clusters as compared with the shallower potentials of NR clusters. At later times, protoclusters grow more due to merging than to smooth accretion. Therefore, large quantities of kinetic motions are brought to the protocluster. The result is that the deepening in the potential caused by cooled baryons is not capable of increasing the virialization process and the result is that both CSF and NR halos get similar values of the virial parameter always higher than 1. The impact of the mass accretion at high redshift was already evident in Fig.10, where it is shown that for CSF objects  $\eta_1$  is more sensitive to the redshift evolution of the total mass.

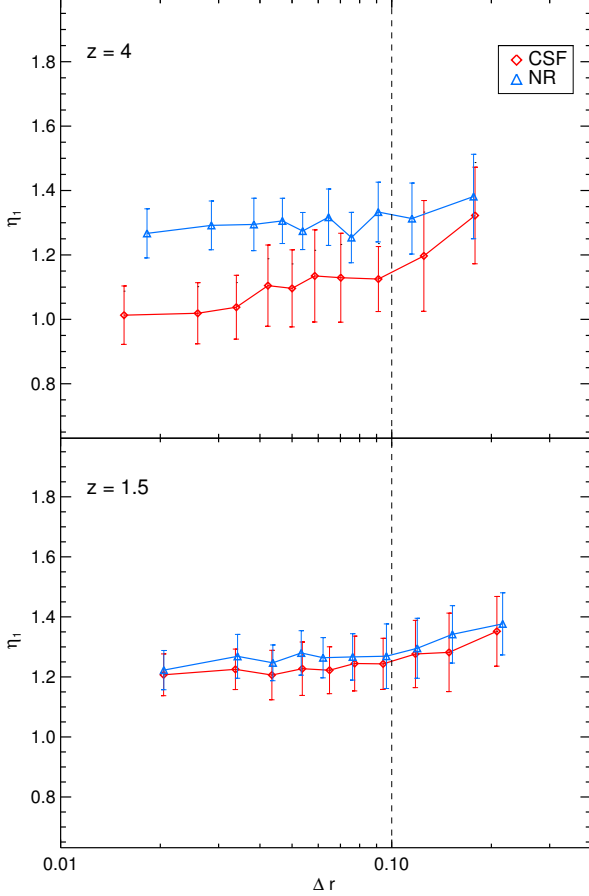


**Figure 9.**  $\eta_1$ - $\Delta r$  relation at  $z = 4$  (top panel) and  $z = 1.5$  (bottom panel). CSF protoclusters (red diamonds) show lower values of  $\eta_1$  than NR protoclusters (blue triangles) at high redshift.

#### 4 THE EXTENSION OF THE Y-M SCALING TO PROTOCLUSTERS

The applicability to protoclusters of scaling relations connecting integrated properties of clusters, such as X-rays luminosity and Sunyaev-Zel'dovich (SZ) effect, has never been investigated. One of the main caveats on this analysis would be the problematics related to the observability of objects at high redshifts (as also discussed in the previous sections of this work).

Here we try for the first time to explore the evolution of the  $Y - M$  scaling relation at  $z > 1$ , with the purpose of checking whether the hypothesis of self-similarity, already well studied for clusters of galaxies, can be applied also to protoclusters.

It has been shown that the integrated thermal SZ effect,  $Y$ , whose definition is recalled here as<sup>6</sup>:

$$Y \equiv \int_{\Omega} y d\Omega = D_A^{-2} \left( \frac{k_b \sigma_T}{m_e c^2} \right) \int_0^{\infty} dl \int_A n_e T_e dA \quad (9)$$

is a robust proxy of the total mass of the cluster, more stable than other proxies in the X-rays band (such as bolometric luminosity and temperature), as it is less affected by the physical processes taking

<sup>6</sup>  $\Omega$  is the solid angle subtended by the cluster,  $D_A$  is the diameter angular distance,  $k_b$  is the Boltzmann constant,  $\sigma_T$  is the Thomson cross section,  $m_e$  is the electron rest mass,  $T_e$  is the electronic temperature and  $n_e$  the numerical density of electrons.

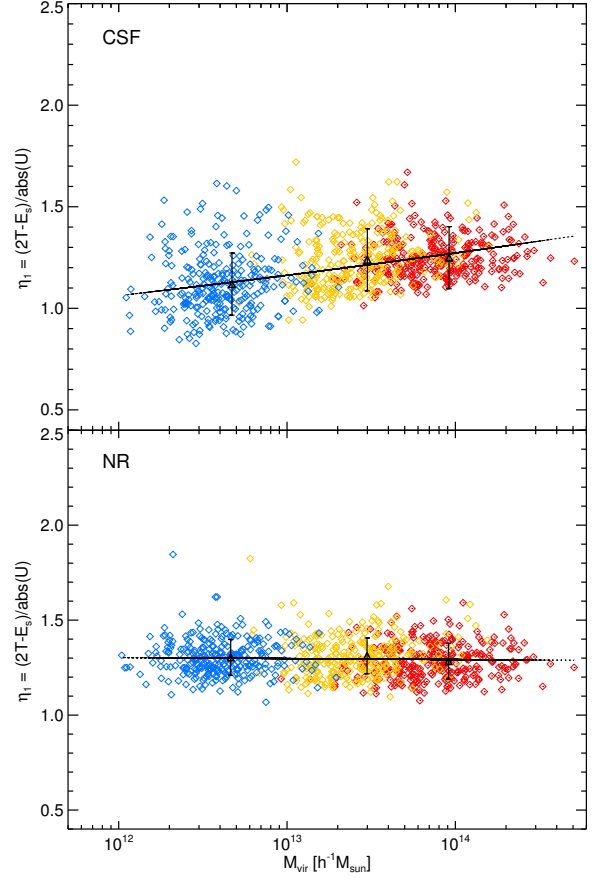


**Figure 10.** Relation between  $\eta_1$  and the mass of the progenitors at different redshifts for CSF protoclusters (top panel) and for NR protoclusters (bottom panel): the first one shows a weak but clear dependence of  $\eta_1$  with mass, the second one does not. Different colors signs objects at different redshifts ( $z = 1.5$  is red,  $z = 2.3$  is yellow and  $z = 4$  is blue). The black line is the best-fit and the black squares show the mean  $\eta_1$  at each redshift.

place in the central regions of clusters. Previous works (Bonaldi et al. 2007, Aghanim, da Silva & Nunes 2009, Kay et al. 2012, Sembolini et al. 2013) have demonstrated that the  $Y - M$  scaling relation, which connects the integrated SZ effect directly to the total mass of the cluster, confirms with good accuracy the hypothesis of self-similarity, showing values extremely close to the self-similar prediction,  $A = 5/3$ .

To estimate the integrated  $Y$  of our dataset of protoclusters we use the same approach already shown in Sembolini et al. (2013), where a detailed analysis of the  $Y - M$  scaling relation for massive clusters of galaxies has been performed in the redshift range  $0 \leq z \leq 1$ . As in the case of massive clusters, we build synthetic maps of the Compton  $y$ -parameter for each protocluster at the different redshifts analyzed and we estimate the  $Y$  value integrated inside the virial radius. The choice of the integration up to the virial radius is motivated by the limited angular resolution of the expected observations towards so far objects.

The  $Y - M$  scaling relation at a fixed overdensity is studied performing a best fit of

$$Y_{\Delta} = 10^B \left( \frac{M_{\Delta}}{h^{-1} M_{\odot}} \right)^A E(z)^{2/3} [h^{-2} Mpc^2] \quad (10)$$

where  $M_{\Delta}$  is the total mass calculated inside the sphere of radius



$r_\Delta$  that we are considering: in our case  $\Delta = \Delta_{vir}$ , so that  $M_\Delta$  corresponds to the total virial mass of the protoclusters. The normalization  $B$  is defined as:

$$B = \log \left[ \frac{\sigma_T}{m_e c^2} \frac{\mu}{\mu_e} \left( \frac{\sqrt{\Delta_c} G H_0}{4} \right)^{2/3} \right] + \log f_g, \quad (11)$$

and contains all the constant terms and the gas fraction (where  $\mu$  and  $\mu_e$  are the mean molecular weights respectively of gas and electrons, see section 4.2 of Sembolini et al. 2013 for more details).

As in the previous section, in the analysis of the  $Y - M$  relation we consider 3 redshifts: 1.5, 2.3 and 4. We find contrasting results. At  $z = 1.5$  (Fig.11) we find a situation comparable to what already observed at  $z \leq 1$ : a slope very close to the self similar value ( $A = 1.69 \pm 0.01$ ), with no substantial differences between NR and CSF subsets, even if objects simulated with non-radiative physics show higher values of  $Y$  and lower slope, as in massive clusters at low redshifts. At  $z = 2.3$  we observe an intermediate situation, with CSF clusters still close to self-similarity ( $A = 1.70 \pm 0.01$ ) but with a normalization which starts to depart from those of NR objects and of the same objects analyzed at  $z < 1$ . At  $z = 4$  (Fig.12) we find that CSF objects show a much stronger deviation from self-similarity ( $A = 1.79 \pm 0.01$ ) and values of  $Y$  (and of the normalization) much smaller than NR protoclusters, whose scaling relation do not exhibit any significant change from  $z = 0$  even at this high redshift.

Various hypothesis can be made to explain this apparently non self-similar behavior of protoclusters at high redshift. Among these we can remind: the effect of disturbed objects on the scaling relation, an incorrect description of the physical processes taking place in the protoclusters or an effect due to the resolution of the simulation.

Aiming at studying the impact of unrelaxed halos on the  $Y - M$  relation, we build two different scaling relations separating relaxed protoclusters from disturbed ones. The results, shown in Fig.13, demonstrate that, as it happens for clusters, the dynamical state of the halos does not affect the  $Y - M$  scaling relation: both relations exhibit a very similar slope well far from the self-similar value. Moreover, it could be observed that neither the fraction of disturbed objects at high redshift does not differ significantly from the one at low redshifts, nor NR protoclusters analyzed at the same redshifts show any deviation from self-similarity even having the same fraction of disturbed objects (around 30 per cent).

The description of the radiative processes used in the simulation has to be taken into account to check the deviation from self-similarity observed at  $z=4$ : in fact, the processes taking place in the protoclusters can be different than those used to model clusters at low redshifts. Moreover, MUSIC simulations do not include AGN feedback, which could play a prominent role on gas physics at high redshifts. On the other hand, we have to consider that the effect of AGNs on clusters is usually that of deviating from self-similar conditions and not to get closer to them: therefore it looks quite unlikely that the presence of AGNs could move the scaling relation of protoclusters towards more self-similar values.

The effect of the resolution of the simulation could constitute a non-physical explanation of the deviation from self-similarity: in fact if we consider the mass resolution of MUSIC simulation this allows us to describe massive clusters (with  $M_{vir} > 5 \times 10^{14} h^{-1} M_\odot$ ) by using several millions of particles. On the contrary, when we move to analyze protoclusters the mass range taken into account is about 3 order of magnitudes smaller (the mean virial mass of our sample at  $z = 4$  is  $5 \times 10^{12} h^{-1} M_\odot$ ), resulting into halos described by only a few ten thousands particles, which may be not

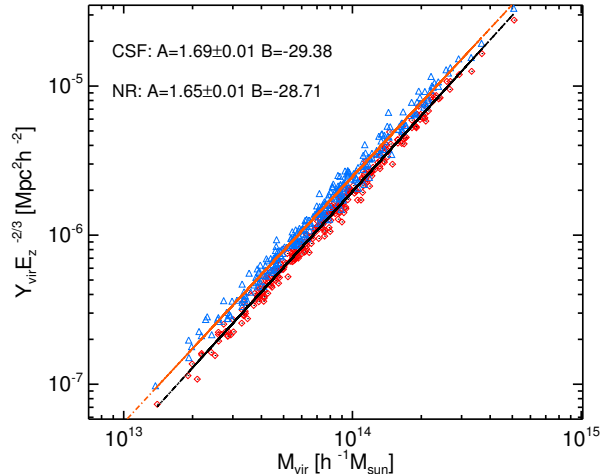


**Figure 11.**  $Y - M$  relation for MUSIC protoclusters at  $z = 1.5$ : CSF protoclusters are represented by red diamonds (the best fit is the black line) and NR protoclusters by blue triangles (the best fit is the orange line).

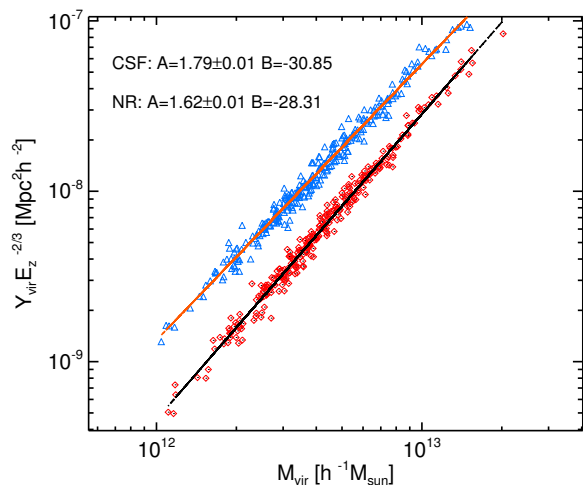


**Figure 12.**  $Y - M$  relation for MUSIC protoclusters at  $z=4.0$ : CSF objects (red diamonds, best fit is the black line) show a clear deviation from self-similarity, NR objects (blue triangles, best fit is the orange line) have a slope still very close to the self-similar value  $A=5/3$ . There is also a big difference between the normalizations of the two subsets.

enough to describe with sufficient precision the integrated properties of protoclusters, such as the integrated  $Y$ . At the same time, NR protoclusters seem, even if constituted by approximately the same number of particles, not to be affected by the same effects of resolution.

Finally, Fig.14 shows the evolution of the slope  $A$  of the  $Y - M$  scaling relation from  $z = 4$  to  $z = 0$ , as result of the analysis at high redshifts discussed in this section joined with the analysis performed for massive clusters (whose progenitors are the protoclusters studied in this work) at  $z \leq 1$  by Sembolini et al. (2013). We notice how, at the virial radius, clusters keep a very good agreement with self-similarity up to  $z=1.5$ , starting to depart from it at  $z > 2$ , to finally show a clear deviation (in the case of objects simulated including radiative processes) at  $z = 4$ . A slight deviation from self-similarity is found also in NR protoclusters.

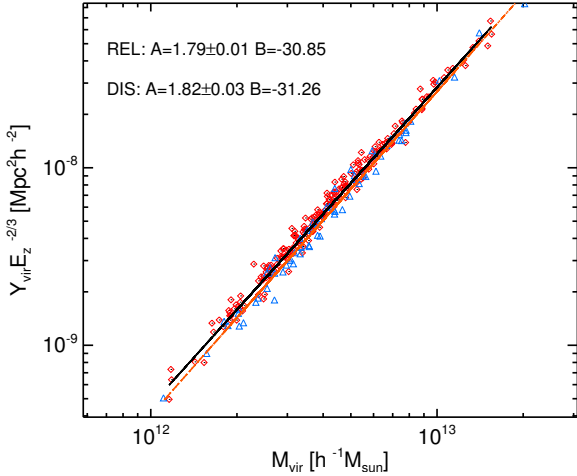


**Figure 13.**  $Y - M$  relation for MUSIC protoclusters at  $z = 4.0$  for CSF objects only, distinguished between relaxed (red diamonds, best fit is the black line) and disturbed (blue triangles, best fit is the orange line) objects.

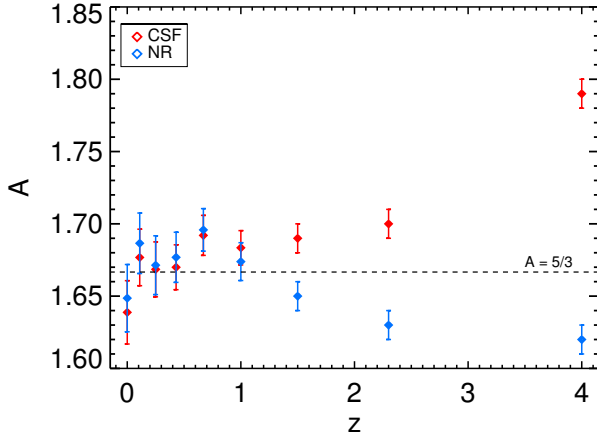


**Figure 14.** Evolution of the slope  $A$  of the  $Y - M$  scaling relation from  $z=0$  to  $z=4$ : values referring to CSF subset are identified by the red diamonds, the NR subset is represented using blue diamonds.

## 5 SUMMARY AND CONCLUSIONS

The study of the progenitors of clusters of galaxies can give a fundamental contribution to better understand how the massive objects that we observe at present time have evolved. The biggest issue related to the analysis of these objects is related to the difficulties of observing them using present experiments and to the rarity of massive objects at  $z > 1$  predicted by the standard  $\Lambda$ CDM model. The use of simulations is therefore crucial to limit this problem, making very easy to individuate the high redshift halos which will evolve into clusters. For the purpose of this work, we adopt the definition of a protocluster as the most massive high redshift progenitor of a galaxy cluster observed at  $z = 0$  and for progenitors as all those high redshift object whose a considerable fraction of mass will be part of the cluster.

Using hydrodynamical simulations of galaxy clusters, here we studied some general properties of protoclusters: the mass and spatial distribution and their redshift evolution, the criteria to distinguish relaxed halos from disturbed ones and the baryon content. We also applied for the first time the study of the  $Y - M$  scal-

ing relation to objects at redshifts higher than 1, comparing the results with those referring to clusters at  $z \leq 1$  reported in Sembolini et al. (2013). Our analysis was performed using MUSIC, the largest dataset of hydrodynamically simulated clusters of galaxies at present available. We concentrated on MUSIC-2, an ensemble of 282 lagrangian regions surrounding massive clusters (usually with  $M_{vir} > 5 \times 10^{14} h^{-1} M_{\odot}$ ) extracted from a big DM only cosmological simulations and resimulated with radiative (CSF subset) and non-radiative (NR subset) physics. We analyzed protoclusters and progenitors of MUSIC clusters at 3 different redshifts,  $z = 1.5, 2.3$  and 4.0. The main results of our work can be summarized as follows:

- At  $z = 4$  only a few protoclusters have  $M > 10^{13} h^{-1} M_{\odot}$ , while at  $z = 1.5$  we already find more than 100 halos with  $M > 10^{14} h^{-1} M_{\odot}$ . At high redshifts, only a fraction (slightly more than 50 per cent at  $z = 1.5$ , less than 15 per cent at  $z = 4$ ) of the mass of the present day cluster is hosted by the progenitors, as most of the mass belongs to diffuse matter or to structure with  $M > 1.2 \times 10^{10} h^{-1} M_{\odot}$ . The study of the spatial distribution of protoclusters shows that the cluster forming region, whose center is individuated by the protocluster, has a mean  $R_{rms}$  that decreases from about  $11 h^{-1} \text{Mpc}$  at  $z = 4$  to  $8 h^{-1} \text{Mpc}$  at  $z = 1.5$ .

- The analysis of the baryon content of protoclusters does not show any crucial difference with the results inferred from simulations of galaxy clusters at  $z < 1$ . The baryon fraction, normalized to the cosmic ratio and calculated inside the virial radius is  $F_b \sim 0.95$  with no redshift evolution. The normalized gas fraction  $F_g$  is ranges from 60 (high redshifts) to 70 per cent (low redshifts) and the star fraction  $F_s$  increases with redshift but always with values lower than 40 per cent: the effects of cold flows in MUSIC are therefore limited also at  $z > 1$ .

- We considered different criteria in order to study the dynamical state of protoclusters and to distinguish the relaxed halos from the disturbed ones. Excluding the effect of mergers, that seems to have a smaller impact on high redshift objects, we concentrated on the virial ratio  $\eta_1$ , corrected including the effect of surface pressure term, and on the spatial shift between the center-of-mass and the center-of-density,  $\Delta r$ . There is a linear relation between the total mass and the virial ratio, observed only in the CSF subset, and objects at  $z = 4$  show values of  $\eta_1$  closer to 1. The two different methods seem to be correlated, as to higher value of  $\Delta r$  correspond higher values of  $\eta_1$ : differently from what observed in DM only simulations, there is a linear dependence between the two parameters. Moreover, the effect of the surface pressure seems to have an impact smaller than in halos simulated only with DM particles. We chose to define as disturbed the ones with  $\Delta r \geq 0.1$ .

- We extended for the first time the analysis of the  $Y - M$  scaling relation to objects redshifts higher than 1. While NR protoclusters seem to be in good agreement with the self similar model up to  $z = 4$ , on the other hand CSF objects seem to show a deviation from self-similarity at  $z > 2$ . The  $Y - M$  relation of CSF clusters at  $z = 4$  has a slope  $A = 1.79$ , well different from the self-similar expected value  $A = 5/3$  and  $Y$  values lower than NR halos. In order to check a possible effect of the dynamical state of objects, we studied the  $Y - M$  relation discerning relaxed protoclusters and disturbed ones. No differences have been found between the two subsets. We also made the hypothesis that the deviation from self-similarity may be due to the mass resolution of the simulation, as protoclusters at  $z = 4$  have masses up to three order of magnitudes smaller than clusters at  $z = 0$ : anyway NR halos, simulated with the same number of particles, do not show any deviation from self-similarity. Another

factor which may contribute to this effect could be an incomplete description of the physical processes taking place inside the proto-clusters (i.e. MUSIC simulations do not include AGN feedback): by the way, these factors are expected to have an opposite effect on scaling relations, moving them away from self-similarity.

To summarize, the use of hydrodynamical simulations to study protoclusters of galaxies seems very promising to better understand the evolution of present day clusters of galaxies and to approach problematics that are challenging with the resolution of present observational instruments. The proposed large-class satellite mission, PRISM (PRISM Collaboration et al. 2013), thanks to the large spectral coverage, angular resolution and sensitivity is expected to deeply explore the universe beyond  $z=2$  planning to detect thousands of objects with  $M > 5 \times 10^{13} M_{\odot}$ . The analysis of many interesting protoclusters' properties, such as the dynamical state, the baryon content or the scaling relations, can be considerably improved when using simulations including gas and star particles with respect to DM only simulations.

In order to double check whether the deviation from self-similarity observed in CSF protoclusters at  $z = 4$  is due to real physical effects or it is just a consequence of the resolution of the simulation, we plan to resimulate MUSIC protoclusters in the range  $1 \leq z \leq 4$ , improving the mass resolution of at least a factor of 8 and eventually adding more physical processes, such as AGN feedback, and using a binning in redshift narrower than the one adopted in this work.

## ACKNOWLEDGEMENTS

The MUSIC simulations were performed at the Barcelona Supercomputing Center (BSC) and the initial conditions were done at the Leibniz Rechenzentrum Munich (LRZ). The authors also thankfully acknowledge the computer resources, technical expertise and assistance provided by the Red Española de Supercomputación. We thank the support of the MICINN Consolider-Ingenio 2010 Programme under grant MultiDark CSD2009-00064. GY acknowledges support from MICINN under research grants AYA2009-13875-C03-02, AYA2012-31101, FPA2009-08958 and Consolider Ingenio SyeC CSD2007-0050. This work has also been partially supported by funding from the University of Rome Sapienza, Anno: 2012 - prot. C26A12T3AJ. FS thanks Alexander Knebe for the useful discussions.

## REFERENCES

- Aghanim N., da Silva A. C., Nunes N. J., 2009, *A&A*, 496, 637  
 Archibald E. N., Dunlop J. S., Hughes D. H., Rawlings S., Eales S. A., Ivison R. J., 2001, *MNRAS*, 323, 417  
 Battaglia N., Bond J. R., Pfrommer C., Sievers J. L., 2011, *ArXiv e-prints* 2011arXiv1109.3709B  
 Bayliss M. B. et al., 2013, *ArXiv e-prints*  
 Birnboim Y., Dekel A., 2003, *MNRAS*, 345, 349  
 Blain A. W., Longair M. S., 1993, *MNRAS*, 264, 509  
 Blain A. W., Smail I., Ivison R. J., Kneib J.-P., Frayer D. T., 2002, *Phys. Rep.*, 369, 111  
 Bonaldi A., Tormen G., Dolag K., Moscardini L., 2007, *MNRAS*, 378, 1248  
 Bonamente M., Joy M., LaRoque S. J., Carlstrom J. E., Nagai D., Marrone D. P., 2008, *ApJ*, 675, 106  
 Capak P. L. et al., 2011, *Nature*, 470, 233  
 Chandrasekhar S., 1961, *Hydrodynamic and hydromagnetic stability*. Oxford  
 Dekel A. et al., 2009, *Nature*, 457, 451  
 Dolag K., Reinecke M., Gheller C., Imboden S., 2008, *New Journal of Physics*, 10, 125006  
 D'Onghia E., Navarro J. F., 2007, *MNRAS*, 380, L58  
 Giavalisco M., 2002, *ARA&A*, 40, 579  
 Hatch N. A. et al., 2011, *MNRAS*, 410, 1537  
 Kay S. T., Peel M. W., Short C. J., Thomas P. A., Young O. E., Battye R. A., Liddle A. R., Pearce F. R., 2012, *MNRAS*, 422, 1999  
 Kereš D., Katz N., Weinberg D. H., Davé R., 2005, *MNRAS*, 363, 2  
 Knebe A., Power C., 2008, *ApJ*, 678, 621  
 Knollmann S. R., Knebe A., 2009, *ApJS*, 182, 608  
 Kuiper E. et al., 2010, *MNRAS*, 405, 969  
 Macciò A. V., Dutton A. A., van den Bosch F. C., Moore B., Potter D., Stadel J., 2007, *MNRAS*, 378, 55  
 Madau P., Diemand J., Kuhlen M., 2008, *ApJ*, 679, 1260  
 Marriage T. A. et al., 2011, *ApJ*, 737, 61  
 Marrone D. P. et al., 2012, *ApJ*, 754, 119  
 Matsuda Y. et al., 2009, *MNRAS*, 400, L66  
 Mayo J. H., Vernet J., De Breuck C., Galametz A., Seymour N., Stern D., 2012, *A&A*, 539, A33  
 Miley G., De Breuck C., 2008, *A&A Rev.*, 15, 67  
 Pierini D. et al., 2012, *A&A*, 540, A45  
 Planck Collaboration et al., 2013a, *ArXiv e-prints*  
 Planck Collaboration et al., 2013b, *ArXiv e-prints*  
 Planck Collaboration et al., 2013c, *A&A*, 550, A129  
 Planck Collaboration et al., 2011, *A&A*, 536, A8  
 Planelles S., Borgani S., Dolag K., Ettori S., Fabjan D., Murante G., Tornatore L., 2013, *MNRAS*, 431, 1487  
 Power C., Knebe A., Knollmann S. R., 2012, *MNRAS*, 419, 1576  
 Prada F., Klypin A. A., Cuesta A. J., Betancort-Rijo J. E., Primack J., 2012, *MNRAS*, 423, 3018  
 PRISM Collaboration et al., 2013, *ArXiv e-prints*  
 Reichardt C. L. et al., 2013, *ApJ*, 763, 127  
 Rocca-Volmerange B., Le Borgne D., De Breuck C., Fioc M., Moy E., 2004, *A&A*, 415, 931  
 Santos J. S. et al., 2011, *A&A*, 531, L15  
 Sembolini F., Yepes G., De Petris M., Gottlöber S., Lamagna L., Comis B., 2013, *MNRAS*, 429, 323  
 Seymour N. et al., 2012, *ApJ*, 755, 146  
 Seymour N. et al., 2007, *ApJS*, 171, 353  
 Shaw L. D., Holder G. P., Bode P., 2008, *ApJ*, 686, 206  
 Shaw L. D., Weller J., Ostriker J. P., Bode P., 2006, *ApJ*, 646, 815  
 Sifón C. et al., 2013, *ApJ*, 772, 25  
 Springel V., 2005, *MNRAS*, 364, 1105  
 Springel V. et al., 2005, *Nature*, 435, 629  
 Staniszewski Z. et al., 2009, *ApJ*, 701, 32  
 Steidel C. C., Adelberger K. L., Dickinson M., Giavalisco M., Pettini M., 1998, *ArXiv Astrophysics e-prints*  
 Steidel C. C., Adelberger K. L., Shapley A. E., Pettini M., Dickinson M., Giavalisco M., 2000, *ApJ*, 532, 170  
 Stevens J. A. et al., 2003, *Nature*, 425, 264  
 Sun M., Sehgal N., Voit G. M., Donahue M., Jones C., Forman W., Vikhlinin A., Sarazin C., 2011, *ApJ*, 727, L49  
 Sunyaev R. A., Zeldovich Y. B., 1970, *Ap&SS*, 7, 3  
 Venemans B. P. et al., 2007, *A&A*, 461, 823  
 Williamson R. et al., 2011, *ApJ*, 738, 139  
 Wylezalek D. et al., 2013, *MNRAS*, 428, 3206

Yamada T., Nakamura Y., Matsuda Y., Hayashino T., Yamauchi R., Morimoto N., Kousai K., Umemura M., 2012, AJ, 143, 79

This paper has been typeset from a T<sub>E</sub>X/L<sup>A</sup>T<sub>E</sub>X file prepared by the author.